Biomedicine & Pharmacotherapy 166 (2023) 115404

Contents lists available at ScienceDirect

Biomedicine & Pharmacotherapy

journal homepage: www.elsevier.com/locate/biopha

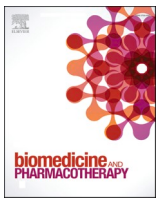

Uncovering the dynamics of cellular responses induced by iron-carbohydrate complexes in human macrophages using quantitative proteomics and phosphoproteomics

Jonas Bossart [a,b,c], Alexandra Rippl [a], Amy E. Barton Alston [d], Beat Flühmann [d], Reinaldo Digigow [d], Marija Buljan [a,b], Vanesa Ayala-Nunez [a,*], Peter Wick [a,*]

[a] Empa, Swiss Federal Laboratories for Materials Science and Technology, Particles-Biology Interactions Laboratory, CH-9014 St. Gallen, Switzerland
[b] SIB, Swiss Institute of Bioinformatics, CH-1015 Lausanne, Switzerland
[c] ETH Zurich, Department of Health Sciences and Technology (D-HEST), CH-8093 Zurich, Switzerland
[d] CSL Vifor, CH-8152 Glattbrugg, Switzerland

ARTICLE INFO

Keywords:
Quantitative proteomics
Phosphoproteomics
Iron-carbohydrate complexes
Iron metabolism
Macrophages

ABSTRACT

Iron-carbohydrate complexes are widely used to treat iron deficiencies. Macrophages play a crucial role in the uptake and fate of these nanomedicines, however, how complexed iron carbohydrates are taken up and metabolized by macrophages is still not fully understood. Using a (phospho-)proteomics approach, we assessed differences in protein expression and phosphorylation in M2 macrophages triggered by iron sucrose (IS). Our results show that IS alters the expression of multiple receptors, indicative of a complex entry mechanism. Besides, IS induced an increase in intracellular ferritin, the loss of M2 polarization, protective mechanisms against ferroptosis, and an autophagic response. These data indicate that macrophages can use IS as a source of iron for its storage and later release, however, the excess of iron can cause oxidative stress, which can be successfully regulated by the cells. When comparing IS with ferric carboxymaltose (FCM) and iron isomaltoside-1000 (IIM), complexes with a higher carbohydrate ligand stability, we observed that FCM and IIM are metabolized at a slower rate, and trigger M2 polarization loss to a lower extent. These results indicate that the surface characteristics of the iron-carbohydrate complexes may influence the cell responses. Our data show that the application of (phospho-)proteomics can lead to a better understanding of metabolic processes, including the uptake, biodegradation and bioavailability of nanomedicines.

1. Introduction

Intravenous (IV) iron-carbohydrate complexes are an established part of current treatment regimens for iron deficiency (e.g. in patients with chronic kidney disease, heart failure or inflammatory bowel disease) and are an indispensable part of clinical treatment [1–4]. These complexes are nanoparticles where polynuclear iron-oxyhydroxide cores are complexed with specific carbohydrate ligands and do not occur naturally in the human body, although they are designed to mimic the structure of serum ferritin [5]. Iron sucrose (IS) was the first iron-carbohydrate complex approved for patient treatment (1949). Nowadays, several products are available globally, including more stable iron-carbohydrate complexes with ligands such as isomaltoside and carboxymaltose. The clinical data and market approval of the multiple iron-carbohydrate complexes have clearly demonstrated favorable efficacy and safety profiles in terms of risk-benefit ratio [6–8].

Clinical and experimental data from in vivo and in vitro studies have given a general understanding of the main events taking place post-injection of these drugs. In the clinical setting, it has been observed that after IV administration, iron is found in storage sites mainly in the liver and spleen, from where it is gradually released to the bone marrow [9]. The iron-carbohydrate complexes are cleared from circulation with a half-life ($t_{1/2}$) of 3.43–20.3 h (depending on the product), blood transferrin is saturated at 2–24 h, and maximal serum ferritin levels are reached after 36–96 h [10]. After clearance from the blood compartment, the iron is stored in the mononuclear phagocytic system (MPS), and macrophages (e.g. Kupffer cells in the liver) are presumed to function as the key players in the uptake and biodegradation of the

* Corresponding authors.
E-mail addresses: vanesa.ayala@empa.ch (V. Ayala-Nunez), peter.wick@empa.ch (P. Wick).

https://doi.org/10.1016/j.biopha.2023.115404
Received 22 June 2023; Received in revised form 22 August 2023; Accepted 28 August 2023

iron-carbohydrate complexes [11]. In vitro studies have shown that iron-carbohydrate complexes, like IS, can activate macrophages and dendritic cells, and potentially affect their phagocytic activity and differentiation process [12,13]. However, these studies did not unravel the effect and mode of action of these nanomedicines at the cellular and molecular level post-injection. In particular, the mechanism of how macrophages internalize the nanoparticles, how these cells metabolize the nanoparticles and use them as a source of iron, and the impact of the nanoparticles on macrophages, has not been fully characterized.

An important factor to understand the mode of action of iron-carbohydrate complexes are their physicochemical properties, in particular, the carbohydrate ligands bound to the polynuclear iron cores. Besides the carbohydrate ligand itself, the main products on the market vary in terms of pH, bond formation, and particle size (8.3 – 23.6 nm) [5,14]. It has been suggested that the carbohydrate ligand is a main determinant in the pharmacokinetic (PK) and pharmacodynamic (PD) properties of the nanoparticles as well as in their in vivo iron bioavailability [2,5,10]. It is proposed that iron-carbohydrate complexes like IS have a more dynamic interaction with the carbohydrate ligand that allows for some dissociation of iron from the complex post-IV injection, resulting in lower tolerability in patients and limiting the total dose that can be administered [15].

The main objective of this study is to identify potential key players in the biodegradation of iron-carbohydrate complexes in macrophages. In other words, to decipher how these cells take up, use, and transfer the iron to intracellular storage sites. To that end, we performed proteomics and phosphoproteomics analyses of primary human M2 macrophages treated in vitro with iron-carbohydrate complexes. We focused on IS, as it has been the most widely used iron-carbohydrate complex, of which there are multiple generic forms available worldwide [5]. A cross-sectional comparison between IS, ferric carboxymaltose (FCM), and iron isomaltoside-1000 (IIM) was done at one treatment time point. The two latter products are newer than IS (approved within the last 15 years) and their higher molecular weight carbohydrate ligands interact more strongly with the ferric oxyhydroxide cores, compared to IS [5].

This study provides the first proteomic and phosphoproteomic characterization of the response of primary human macrophages to IV iron-carbohydrate complexes and provides extensive molecular insights into the impact these nanomedicines have on the iron-related metabolism.

2. Materials and methods

2.1. Differentiation and polarization of primary human macrophages

Human primary monocytes were purified from buffy coats of healthy adult donors, which were supplied by the blood bank in Zurich, Switzerland (ethical approval BASEC Nr. Req_2021 −00687). A density gradient centrifugation with Ficoll (Sigma-Aldrich) was used to isolate peripheral blood mononuclear cells (PBMCs) from the buffy coats. The monocytes were then negatively selected with a Classical Monocyte Isolation Kit (Miltenyi Biotec).

Following selection, the monocytes were differentiated and polarized into the M1 or M2 macrophage states. For M1 macrophages, the cells were first incubated for 7 days at 37 °C with RPMI-1640 (Sigma-Aldrich) containing 10% fetal calf serum (FCS), 1% penicillin-streptomycin (PS), and 20 ng×mL^{-1} of GM-CSF (Sigma-Aldrich). On day 7, the cell culture media was replaced with fresh media containing 100 ng×mL^{-1} of LPS (Sigma-Aldrich) and 20 ng×mL^{-1} of IFN-γ (Sigma-Aldrich) instead of GM-CSF, and the cells were further incubated for 2 days. In the case of M2 macrophages, the monocytes were initially treated for 7 days with 20 ng×mL^{-1} of M-CSF (Gibco), then for 2 days with IL-4 (20 ng×mL^{-1}) and IL-13 (20 ng×mL^{-1}) (Miltenyi Biotec).

2.2. Iron-carbohydrate complexes

The treatments with iron-carbohydrate complexes were prepared with IS (Venofer®, Lot No. 975101A, Vifor (International) Inc.), FCM (Ferinject®, Lot No. 8742012AVB, Vifor (International) Inc.) or IIM (MonoFer®, Lot No. 157633–3, Pierre Fabre Pharma AG). The day of the experiments, aliquots were taken out of the closed vials with a syringe to avoid oxidation. The three different iron-carbohydrate complexes were then diluted in RPMI-1640 10% FCS, 1% PS, at a concentration of 1800 μM of total iron. This concentration is equivalent to the expected plasma concentration of iron after infusion in patients of 300 mg of IS, which corresponds to the clinically relevant iron concentration [16].

2.3. Inductively Coupled Plasma - Optical Emission spectroscopy (ICP-OES)

ICP-OES was used to quantify total iron in the cells. Human primary monocytes were plated in 12-well plates at a cell density of 500,000 cells/well. The monocytes were differentiated and polarized either to M1 or M2 macrophages as described previously. Once fully polarized, the cells were treated for 6 h with IS, FCM or IIM, at an iron concentration of 1800 μM. After treatment, the cells were washed three times with DPBS -/- (Sigma-Aldrich), and lysed by incubating them for 20 min at 4 °C with RIPA Buffer (Sigma-Aldrich). Before processing for ICP-OES, 70 μL of each sample were taken for DNA quantification.

The rest of the sample volume was added to a Teflon tube suited for microwave digestion and 440 μL of 68% HNO_3 was added. The tubes were microwaved and 500 μL of fresh H_2O_2 suited for elemental analysis was added per sample. Afterwards, the samples were transferred into a 15 mL falcon tube and diluted with MilliQ water. The calibration standards were prepared in 2% HNO_3 from 1 to 10,000 ppb by appropriate dilutions of the ionic Fe stock solution. Iron content measurements were done with the axial measurement mode with a 5110 ICP-OES (Agilent Technologies) instrument.

In parallel, total DNA was quantified using a Quant-iT™ PicoGreen™ dsDNA Assay Kit (ThermoFisher) by following the manufacturer's instructions. The DNA value (in pg) was used to quantify the total amount of iron per cell (pg Fe/cell) by normalizing the total iron content by the DNA content of the samples. It was assumed that one cell has 6 pg of DNA.

2.4. Prussian Blue-DAB staining

Perls Prussian Blue is a widely used staining used to detect the presence of ferric iron (Fe^{3+}) in fixed cells and tissues. Additionally, we performed a staining with 3,3'-diaminobenzidine to enhance the signal of the Prussian Blue staining [17].

To prepare the sample, human primary monocytes were plated in 96-well plates at a cell density of 50,000 cells/well. The monocytes were differentiated to M2 macrophages as described previously. Once fully differentiated, the cells were treated with IS, FCM or IIM with an iron concentration of 1800 μM for the indicated time points. After treatment, the cells were washed three times with DPBS and fixed with PFA 4% for 20 min at room temperature (RT). Alternatively, the cells were seeded on a coverslip in a 24-well plate at a cell density of 250,000 cells/well.

The fixed cells were then treated with a freshly prepared Perls Prussian Blue reagent (4% potassium ferrocyanide / 12% HCl, 1:1 vol/volume ratio) for 30 min at RT. The cells were washed three times with DPBS.

For the DAB step, the cells were treated with 0.05% DAB (Sigma Aldrich) in DPBS for 10 min at RT. Then, the solution was removed and a freshly made solution with 0.033% H_2O_2 and 0.05% DAB in DPBS, was added for 10 min at RT. The cells were washed three times with DPBS and imaged. The presence of ferric iron in the cells was observed as a brown precipitate.

2.5. Mass spectrometry

2.5.1. Sample preparation

Human primary monocytes of four healthy donors were plated in T75 flasks at a cell density of 7.5 x 10^6 cells/flask. The monocytes were differentiated to M2 macrophages as described in the previous section. Once fully differentiated, the cells were treated for 45 min, 6 h or 24 h with IS (iron concentration of 1800 μM) in RPMI-1640 10% FCS, 1% PS. Alternatively, the cells were treated for 6 h with FCM or IIM at the same concentration.

After treatment, the cells were washed with DPBS, detached using a cold DPBS solution with 10 mM EDTA (Sigma-Aldrich), followed by a mechanical step with a cell scrapper (VWR). For each measuring point, four treated and four untreated biological replicates were prepared, snap frozen and sent on dry ice to the Functional Genomics Centre Zurich (FGCZ) for proteomic and phosphoproteomic measurements.

After adding 100 μL of FASP lysis buffer to each sample (4% SDS, 100 mM Tris / HCL pH 8.2), the cells were sonicated for 1 min at the highest amplitude using high intensity focused ultrasound (HIFU). The samples were incubated at 95 °C for 10 min, followed by a second HIFU step. A total of 140 μg of protein were reduced with 2 mM TCEP (tris(2-carboxyethyl)phosphine) and alkylated with 15 mM chloroacetamide at 30 °C for 30 min. Protein concentrations were determined on a Lunatic UV/Vis polychromatic spectrophotometer (Unchained Labs). Using a KingFisher Flex System (ThermoFisher Scientific) and Carboxylate-Modified Magnetic Particles (GE Life Sciences), the samples were purified and digested, followed by a peptide clean-up according to the single-pot solid-phase enhanced sample preparation (SP3) protocol [18,19]. Following the manufacturer's instructions, the beads were conditioned with 3 water washes at a concentration of 1 $\mu g \times \mu L^{-1}$. The samples were diluted with 100% ethanol to a final concentration of 60% ethanol. The loading was done on 96 deep well- or micro-plates. On the KingFisher robotic system, the steps were carried out in the following order: bead collection from the last wash, protein-bead binding, washing in wash solutions 1–3 (80% ethanol), protein digestion with a trypsin: protein ratio of 1:50 in 50 mM Triethylammoniumbicarbonat (TEAB) overnight at 37 °C, and peptide elution using MilliQ water. Afterwards, the digest and water elutions were combined. A small aliquot was removed, dried and dissolved in 20 μL of MS sample buffer (3% acetonitrile, 0.1% formic acid) for the full proteome analysis. The remaining samples were dried, solubilized in 150 μL of Fe-NTA binding buffer (80% ACN, 5% TFA), and subjected to the phosphopeptide enrichment protocol as described in published protocols with Fe-NTA beads (Cube Biotech) at a bead:peptide ratio of 10:1 [18,19].

2.5.2. Data acquisition

The samples were analyzed on an Orbitrap Fusion Lumos (Thermo Scientific) equipped with a Digital PicoView source (New Objective), which was coupled to a M-Class UPLC (Waters). The analyses were conducted in randomized order for each sample individually. Thereby, 1–2 μL of dried peptides or 50% of the dried Fe-NTA elution samples were used for the whole proteome and phosphoproteome analyses, respectively. The column temperature was set to 50 °C and the channels equipped with either solvent A (0.1% formic acid) or solvent B (99.9% acetonitrile in 0.1% formic acid). The samples were loaded on a trap column (Waters ACQUITY UPLC M-Class Symmetry C18 Trap Column; 100 Å, 5 μm, 180 μm × 20 mm), which was followed by a second column (Waters ACQUITY UPLC M-Class HSS T3 Column; 100 Å, 1.8 μm, 75 μm × 250 mm). A constant flow rate of 300 $nL \times min^{-1}$ was selected. The elution got started with a 3 min hold at 5% B, which was followed by a gradient increase to 22% B in 80 min and then to 32% B in 10 min. Before loading conditions were re-established, the column was cleaned by increasing to 95% solvent B and holding this composition for 10 min. With a maximum cycle time of 3 s, the spectrometer was operated in data-dependent acquisition (DDA) mode, while setting spray voltage to 2.6 kV, funnel RF level to 40%, heated capillary temperature to 275 °C, and Advanced Peak Determination (APD) on. After accumulation to an automated gain control (AGC) target value of 500,000 or for a maximum injection time of 50 ms full-scan MS spectra (300 −1500 m/z) were acquired at a resolution of 120,000 at 200 m/z. Precursors exceeding an intensity of 5000 were selected for MS/MS, where ions were isolated using a quadrupole mass filter with 0.8 m/z isolation window and further fragmented by higher energy collisional dissociation (HCD) using a normalized collision energy (NCE) of 35%. With the scan rate set to rapid, the AGC set to 10,000 ions, and the maximum injection time set to 50 ms (200 ms for phosphopeptide analysis) the fragments were detected in the linear ion trap. It was decided to enable charge state screening, to exclude singly, unassigned charge states, and charge states higher than seven. Precursor masses, which were previously selected for MS/MS measurement, were excluded from further selection for 20 s, applying a mass tolerance of 10 ppm. The samples were acquired using internal lock mass calibration on m/z 371.1012 and 445.1200. The mass spectrometry data were handled using the local laboratory information management system (LIMS) at the FGCZ [20].

2.5.3. Data analysis

MS data were processed in MaxQuant (version 2.0.1.0) using the integrated Andromeda search engine to identify proteins [21]. Here, the data were searched against a UniProt Homo sapiens reference (taxonomy 9606, canonical version from 2022 to 04–29), concatenated to its reversed decoyed fasta database and common protein contaminants [22]. While carbamidomethylation of cysteine amino acids was set as fixed modification, methionine oxidation, N-terminal protein acetylation and phospho STY was set as variable. Settings for minimal peptide length of 7 amino acids and a maximum of two missed-cleavages were introduced with an enzymatic specificity set to trypsin/P. The maximum false discovery rate (FDR) was set to 0.05 for proteins and 0.01 for peptides. Label-free quantification (LFQ) was enabled with a 2 min window for match between runs.

2.6. Quantification and statistics

2.6.1. Data cleaning

For the cleaning, processing, and analysis of the MaxQuant outputs, Python and the server-client application Jupyter notebook were used [21,23–25]. Analyses were conducted on the protein and phosphopeptide level. The PaDuA library was used to read the data and transform it into a pandas DataFrame [26,27]. Operations were performed with NumPy [28]. In a first cleaning step, commonly occurring contaminants (fasta file provided by MaxQuant) and entries matching the reversed part of the decoy database were excluded from the analysis. Additional filtering steps were implemented in order to exclude proteins identified only by modification sites or based on single peptides. For phosphopeptides, only entries with a localization confidence above 75% and a posterior error probability below 1% were retained. In addition, entries considered for the downstream analyses were required to have been measured in at least two biological replicates in one of the conditions.

2.6.2. Data transformation, imputation, and normalization

The LFQ values were $Log_2(x)$ transformed. Next, missing data entries were imputed separately for each sample by randomly sampling from the lower range of the measured LFQs values. For this, a normal distribution was constructed with a negative shift of 1.4 standard deviations (SD) from the mean of the actually measured values and with a width of 0.4 SD of the measured values by using the PaDuA library [26]. Following imputation, values were quantile normalized across all analyzed samples.

2.6.3. Differential expression analysis

Protein expression and peptide phosphorylation levels in the biological replicates of the treated samples were compared to those in the untreated ones. For this, two-tailed *t*-tests were implemented using the

SciPy library with a p-value significance threshold of 0.05 [29]. Changes with a $|\text{Log}_2(\text{FC})| \geq 1$ were retained for further analyses. In addition, proteins and phosphopeptides that were uniquely present in one of the conditions were added to the list of significantly differentially regulated proteins. For this, a protein or a phosphopeptide had to be measured in at least three out of four replicates within a condition and be completely absent in the comparison group. These unique entries were excluded from the imputation described above. Proteins and phosphopeptides with significant differences in their expression levels were illustrated using volcano plots (matplotlib [30]) and overlaps among the significant hits were shown using Venn diagrams (Venny [31]). Illustrations were further adjusted in CorelDRAW (https://www.coreldraw.com/).

2.6.4. Analysis of cellular pathways over-represented among significant hits

Next, functional enrichments were assessed among the significant proteins and phosphopeptides, where phosphopeptides coming from the same protein were all represented with the respective protein identifier. The lists of significantly up- or downregulated entries (including unique entries) were analyzed using the CPDB [32] webserver and by assessing enrichment in Reactome [33] and KEGG [34] pathways applying hypergeometric testing. Likewise, the enrichment in Gene Ontology biological processes was analyzed using the DAVID [35] tool for functional annotation, where p-values were calculated by a modified Fisher's exact test. Subsequently, p-values were FDR-corrected according to the Benjamini-Hochberg (BH) method [36]. For the objective analyses, these proteins were compared to the background of all measured proteins or phosphoproteins, as appropriate. Terms with FDR values below 5% were selected. CPDB hits with less than two protein entries, which were not already assigned to a term with higher significance, were not shown as ORA results to reduce redundancy. Figures were created with the matplotlib [30] library and adjusted in CorelDRAW (https://www.coreldraw.com/).

2.6.5. Enrichment analysis of kinase activity

In order to assess enrichment of kinase activities upon treatment two approaches were used: (i) implementation of knowledge on known kinase-substrate pairs and (ii) inference of upstream regulatory kinases based on sequence motifs in the identified phosphopeptides. For the former, the PhosphoSitePlus (PSP) database was used to identify known kinases of up- and downregulated substrates [37], and for the latter, the NetPhorest (NP) algorithm was used [38]. Based on Artificial Neural Networks and Position-Specific Scoring Matrices, this algorithm predicts which kinases are able to recognize sequence motifs surrounding phosphosites and hence phosphorylate the respective residues. Entries with a posterior probability lower than 0.035 and with a posterior probability smaller than the prior probability were removed. For each residue the top three kinases with the highest posterior probability were retained. Fisher's exact tests in the SciPy [29] library were used to identify highly active kinase families. Results for the identified phosphosites were compared to the number of occurrences in the background containing all quantified phosphopeptides. After BH correction of the p-values with the mne library [39], an FDR threshold of 0.05 was implemented. In a second step, the overlap of these indirect and direct evidences was illustrated with the CORAL web application highlighting the data on the kinase dendrogram [40].

2.7. Scheme construction

In order to analyze and visualize molecular changes related to iron in more depth, lists of significant up and down-regulated as well as uniquely identified proteins were extended with what is referred to as iron-related proteins. For this, a relaxed threshold of $|\text{FC}| \geq 1.5$ was introduced. The protein IDs were extracted and matched with a list of IDs of a simple UniProt search for the term *iron*. Enrichment of these proteins was assessed per time point with Fisher's exact tests in the SciPy library [29]. Resulting p-values were BH corrected with the mne library [39]. Significant iron-related hits of an enriched set were compared across all measured time points. Based on an extensive literature search, the most interesting hits were further assessed and highlighted with a main focus on mitochondrial localization, heme metabolism, phagocytosis, transferrin- and other receptor-dependent uptake mechanisms, iron storage, autophagy, and ferroptosis. The illustration in Fig. 6 was created with BioRender (https://biorender.com/).

3. Results

3.1. Iron content of human macrophages increases with IS treatment

Primary human macrophages were differentiated from blood-derived monocytes and polarized into M1 and M2 phenotypes (Fig. 1A). The cells were treated with IS (1800 μM) for 6 h, after which total iron was quantified with ICP-OES. It is important to mention that ICP-OES allows for the quantification of all forms of iron, not specifically the nanoparticles. As observed in Fig. 1B, M2 macrophages exhibited a higher uptake of IS compared to M1 macrophages, although the difference was not statistically evaluated. Together with the fact that M2 macrophages show a higher uptake activity for other nanoparticles [41,42], this supports M2 macrophages as a suitable experimental model for this study. A Prussian Blue-DAB staining showed the presence of Fe^{3+} in the M2 macrophages in a time-dependent manner, confirming that IS treatment effectively drives an increase in the intracellular iron content (Fig. 1C). Cells positive for Fe^{3+} were observed as early as 45 min post-treatment.

For the proteomics and phosphoproteomics analyses, primary human M2 macrophages from four healthy donors were treated with IS for 45 min, 6 h, and 24 h. The decision to perform measurements after 45 min, 6 h, or 24 h treatment was made based on a clinical study, where it was established that IS is mostly cleared from the serum by 24 h post-injection [10]. Hence, the chosen time points will enable insights into early responses to cellular iron uptake and shed light on proteomic changes after completed clearance. The treatment concentration in all conditions was 1800 μM of total iron, corresponding to predicted maximal plasma concentrations in blood after IV administration of iron-carbohydrate complexes.

3.2. IS treatment modifies the proteome and phosphoproteome of M2 macrophages

Untargeted global LFQ of proteins and phosphopeptides was employed to get insights into the differential molecular regulations triggered by IS in a time dependent manner. Using four biological replicates of treated and untreated samples, we identified proteins and phosphopeptides that had statistically significant ($p < 0.05$, $|\text{Log}_2(\text{FC})| \geq 1$) differences in their expression levels. In addition, we included instances present only in one of the studied conditions. This analysis identified several biologically relevant trends, but it also highlighted interindividual variability and differences in the studied processes. In order to retain the insight into dominant processes, the corresponding p-values were not corrected for multiple testing.

By using differential expression analysis (DEA), a total of 121 proteins were identified as differentially expressed upon IS treatment compared to the untreated control (Fig. 2A-D). From these proteins, 77 were unique changes, which we define as protein uniquely present in one of the conditions. The number of proteins identified as differentially expressed increased in a time-dependent manner (27 at 45 min, 49 at 6 h, 51 at 24 h of treatment). Out of the 121 proteins, 115 proteins (95.04%) were exclusively identified as altered at a specific measuring point (Fig. 2A). Proteins that were identified both after 6 h and 24 h of IS treatment are two ferritin chains FTH1 and FTL (higher expression levels compared to untreated samples), three plasma membrane receptors (MSR1, CD209, and STAB1, lower expression levels), and the creatine kinase CKB (lower expression levels).

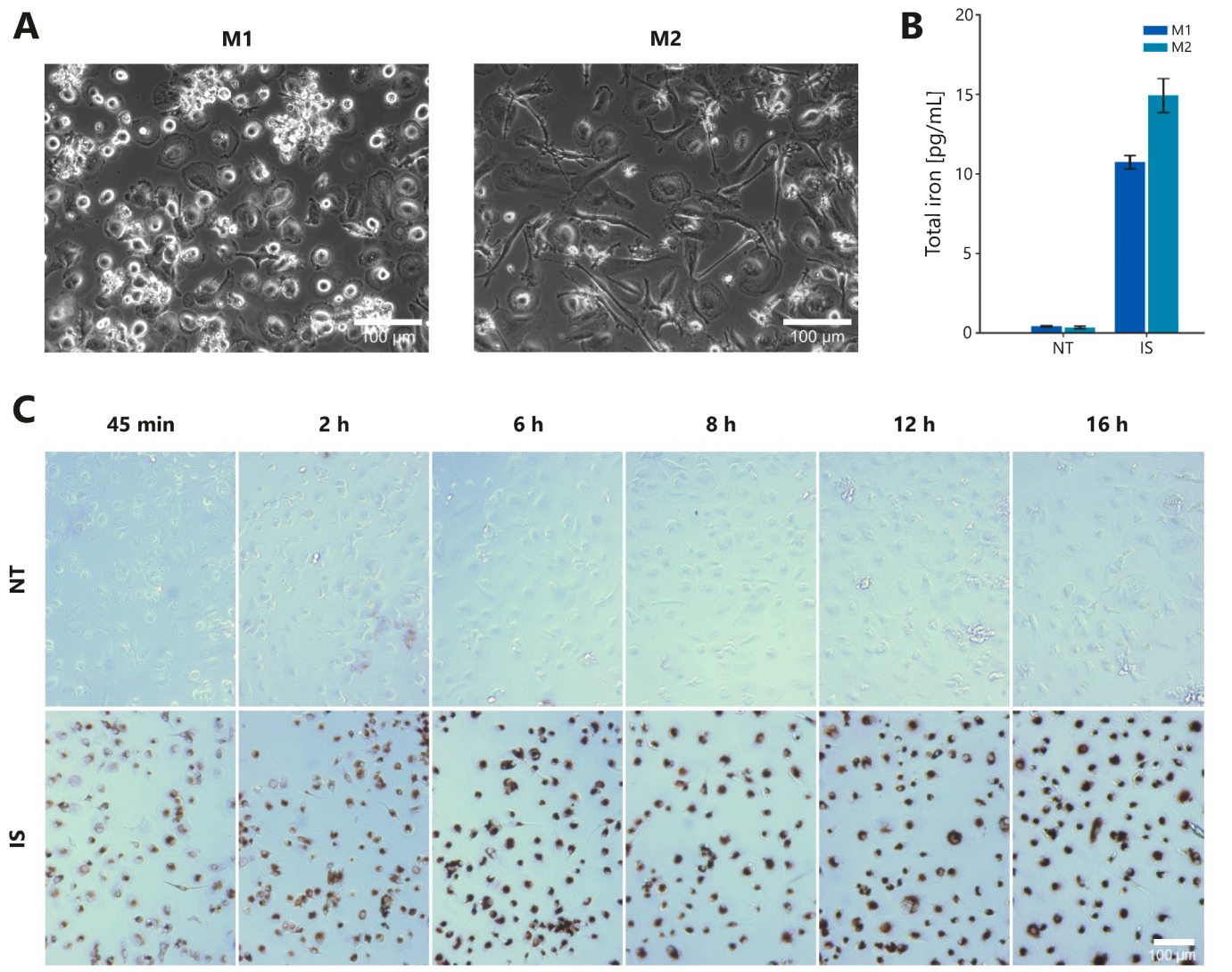

Fig. 1. Human M2 macrophages preferentially take up IS. (A) M1 and M2 macrophages were differentiated and polarized from blood-derived monocytes isolated from buffy coats. Shown are images taken after 7 days of differentiation (M1: GM-CSF, M2: M-CSF) and 2 days of polarization (M1: LPS/IFN-γ, M2: IL-4/IL-13). The images were taken with a Primovert microscope (Carl Zeiss). (B) M1 and M2 human primary macrophages were treated for 6 h with IS (1800 µM). After treatment, the cells were lysed and analyzed with ICP-OES. The DNA content was quantified with a Quant-iT™ PicoGreen™ dsDNA Assay Kit. The total amount of iron per cell is shown (pg Fe/cell). The experiment was done in duplicate with macrophages differentiated from two healthy donors. The graph bars represent the mean and the standard deviation of NT (not treated) and IS (iron sucrose) treated cells. (C) Human M2 macrophages were treated with IS (1800 µM) for the indicated timepoints. The cells were fixed and stained for Fe^{3+} with Perls Prussian Blue and DAB. The brown coloration indicates the presence of Fe^{3+}. Scale bars = 100 µm in (A, C).

A total of 474 phosphoproteins (262 unique) with at least one differentially phosphorylated peptide (Fig. 2E-H) were identified at the three different time points, with 373 (78.7%) of them being specific for a single time point (Fig. 2E). A set of 16 proteins with altered phosphorylation levels were identified at all three measured time points. These phosphoproteins exhibit core cellular functions like RNA-, DNA-, or actin-binding (PDAP1, SRRM1, SRRM2, PALLD, YBX1, DKC1, HMGA1, HDGFL2, PLEC, MYO9B). Additionally, a zinc finger protein (ZC3H13), two hydrolases (EIF5B, VPS4A), a transcription factor (IWS1), and a cytokine (SPP1) were identified in the overlapping protein set. The protein kinase C delta type (PKCD) was found to have highly phosphorylated residues, which are necessary for the kinase activity [43], at the latest two time points (6 h [Thr-507] and 24 h [Ser-664]). Detailed information on proteins with significantly altered expression and phosphorylation levels are listed in the supplementary information (Tables S1 and S2).

The proteomic changes allowed the identification of biological pathways that were significantly altered upon IS treatment. The upregulated pathways are shown in Fig. 2I and J and were obtained by using the Reactome [33] and KEGG [34] databases. The downregulated ones are often represented by broad pathways related to RNA and metabolic processes (Fig. S1A-D). More detailed results of the over-representation analysis (ORA) are listed in Tables S3-S6. The biological pathway *Initiation of Nuclear Envelope Reformation* was specifically identified to be upregulated after 6 h of IS treatment, while *Transport of small molecules* and *Lysosome* related pathways were detected as significant after 24 h. The pathways *Scavenging by Class A receptors* and *Neutrophil degranulation* were upregulated after both 6 and 24 h of IS treatment. After 45 min of IS treatment, there was no significant trend in the upregulation of specific pathways. This reflects not only the influence of the treatment itself, but also the time dependency of the complex altered metabolic pathways, which continue to change even after 24 h.

Among the proteomic hits, the two ferritin heavy (FTH1) and light (FTL) chains clearly stand out due to the high upregulation after an IS treatment for 6 h, and 24 h, respectively. In the clinical setting, serum

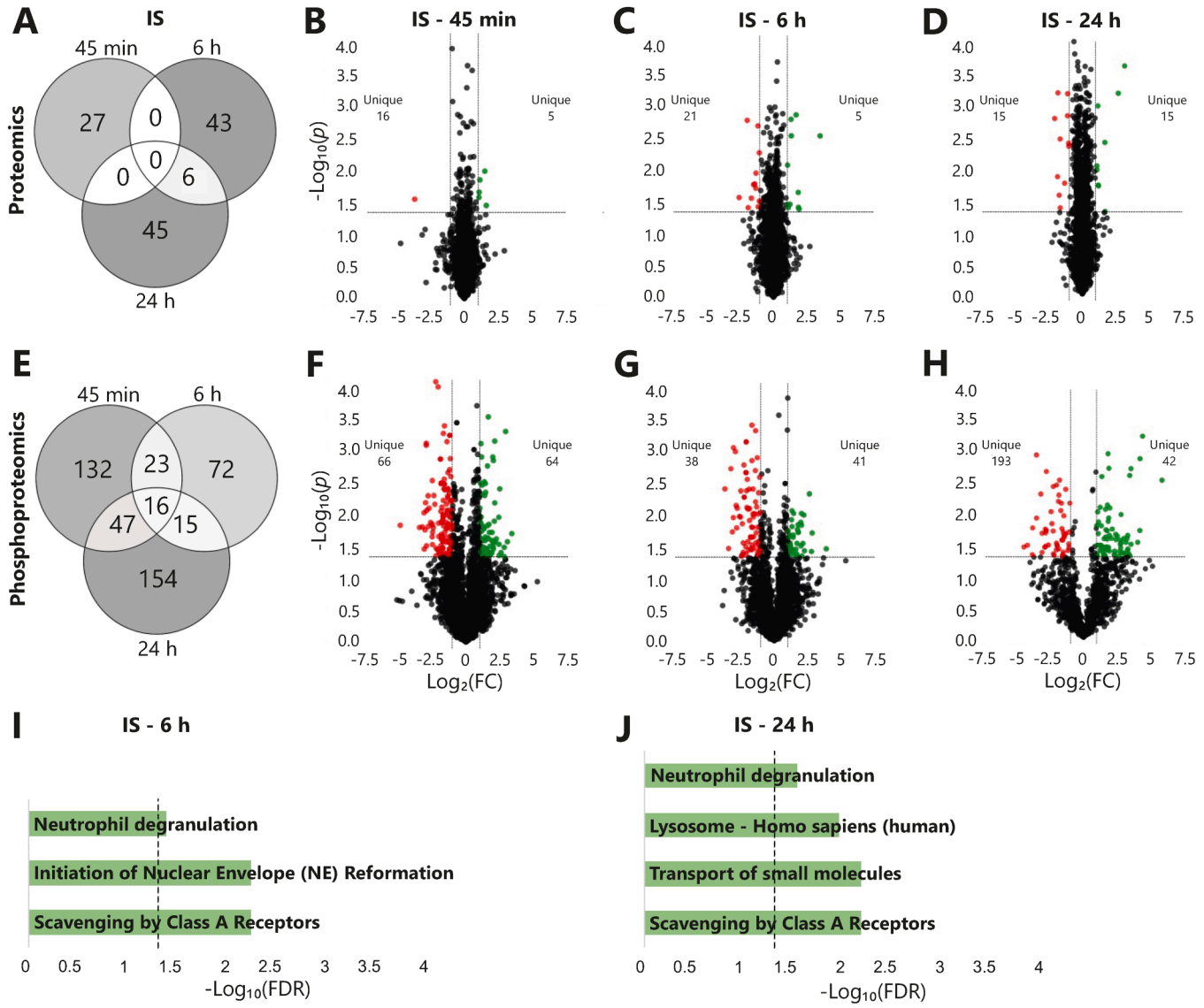

Fig. 2. Changes in M2 macrophage protein expression and phosphorylation after IS treatment. (A) Venn diagram with the numbers of time-specific differentially expressed proteins and corresponding volcano plots after (B) 45 min, (C) 6 h, and (D) 24 h of IS (iron sucrose) treatment. (E) Venn diagram with the numbers of time-specific differentially phosphorylated proteins and corresponding volcano plots on the level of phosphopeptides after (F) 45 min, (G) 6 h, and (H) 24 h of IS treatment. Colored dots (red and green) represent hits with a significant p-value < 0.05 and a $|\text{Log}_2(\text{FC})| \geq 1$ when comparing IS treated with untreated M2 macrophages. Green dots were identified to be upregulated and red dots downregulated hits compared to untreated controls. Significant biological terms derived from the ORA (Reactome [33] and KEGG [34]) of upregulated proteins after (I) 6 h and (J) 24 h of IS treatment. The dashed line represents a significant threshold of an FDR < 0.05.

ferritin is used as an indirect marker of total body iron; hence, it has been used as a PD marker for the transition of iron derived from iron-carbohydrate complexes into iron storage sites [11]. As described, our data show that treatment with IS (6 h) induced the expression of the FTH1 and FTL chains (Fig. 3) with a strong Log_2(FC) of 3.39 and 1.80, respectively. Over the next 18 h, the light chain further increased its expression to a Log_2(FC) of 2.72. The expression of FTH1 was still significantly increased at the later time point ($\text{Log}_2(\text{FC}) = 3.20$). In addition, a phosphopeptide of FTH1 [Ser-179] was found to be upregulated ($\text{Log}_2(\text{FC}) = 1.76$) after 6 h of IS treatment. The heavy and light chains of ferritin are responsible for the over-representation of the biological pathway *Scavenging by Class A Receptors* and partly of the pathways *Neutrophil degranulation*, and *Transport of small molecules* (Fig. 2I-J and Table S4), underlining the importance and varying impacts these two proteins can have on multiple biological pathways.

In addition to the described hits, proteins with a relaxed threshold of $|\text{FC}| \geq 1.5$ ($|\text{Log}_2(\text{FC})| \geq 0.58$), corresponding to a top hit fraction of 2–4% of the quantified proteins, were examined. Iron-related proteins were extracted (see Materials and Methods) and the enrichment among differentially expressed proteins was assessed per time point. In the case of the 6 and 24 h time points, an enrichment of iron-related proteins was observed with Odds values of 2.6 and 2.7, respectively (FDR < 0.05). Significant changes among iron-related proteins in enriched datasets were compared across all measured time points. The most prominent molecular changes were manually selected and discussed in Section 4. Discussion.

3.3. Regulation of protein expression and phosphorylation is carbohydrate-dependent

In a cross-sectional approach, proteomic and phosphoproteomic changes in M2 macrophages were compared upon treatment with IS, FCM, and IIM. IIM has carbohydrate ligands composed of a reduced linear chemical structure of repeating α1–6 linked glucose units, with an

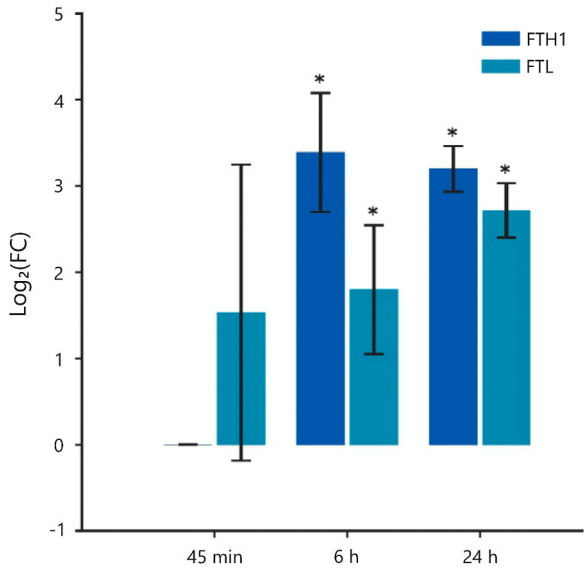

Fig. 3. Changes in the expression of FTH1 and FTL ferritin chain proteins upon IS (iron sucrose) treatment. The bar graphs show the mean Log_2(FC) with standard deviations of four biological replicates. The stars highlight significant changes ($p < 0.05$) of treated versus untreated samples.

average molecular weight of 1000 Da [14]. The ligand carboxymaltose is obtained from maltodextrin by oxidation and it is composed of 1→4-linked maltose polysaccharides with carboxylic acid [5]. The 6 h time point was chosen because the clinical data of IS show a partial serum clearance of the complex and, at the same time, a modest increase in serum ferritin, indicating that the iron has already been metabolized to a certain extent [10]. This assures that the primary cellular responses to iron are being compared.

We first confirmed that FCM and IIM increased the iron content in M1 and M2 macrophages. As with IS, primary human M1 and M2 macrophages from different donors were treated with 1800 μM of FCM and IIM for 6 h. Total iron was quantified with ICP-OES (Fig. 4). Our data indicate that both iron-carbohydrate complexes are preferably taken up by M2 macrophages, though to a lower extent compared to IS (Fig. 1B), and thus verifying the selection of the M2 macrophages as the main experimental model also for the comparison of the treatment responses to IS, FCM, and IIM.

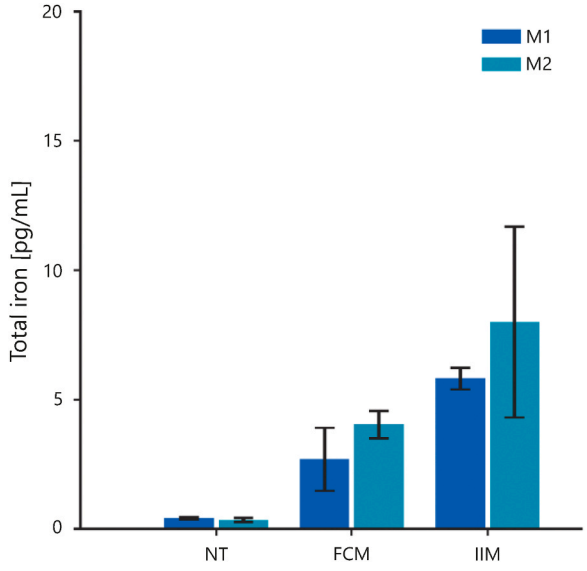

Fig. 4. Human macrophages take up FCM and IIM. M1 and M2 human primary macrophages were treated for 6 h with FCM and IIM (1800 μM of total iron). After treatment, the cells were lysed and analyzed with ICP-OES. The DNA content was quantified with a Quant-iT™ PicoGreen™ dsDNA Assay Kit. The total amount of iron per cell is shown (pg Fe/cell). The experiment was done in duplicate with macrophages differentiated from two healthy donors. The graph bars represent the mean and the standard deviation of NT (not treated), FCM (ferric carboxymaltose) and IIM (iron isomaltoside-1000) treated cells.

On a molecular level, more changes in protein abundances were triggered by a 6 h treatment with IS (49 proteins), compared to FCM (26 proteins) and IIM (19 proteins) (Figs. 2C and 5A-C). It was observed that 15 out of a total of 76 altered proteins (19.74%) were differentially regulated upon the treatment with all three products, with the remaining 61 proteins being specific to one product (Fig. 5A). In each case, the unique presence of the transferase CDIPT was observed in comparison to untreated macrophages. This transferase catalyzes the biosynthesis of phosphatidylinositol (PtdIns) [44]. All three iron-carbohydrate complexes lead to the downregulation of OGFRL1, a less-characterized paralog of the opioid growth factor [45], and RASAL2, an inhibitory regulator of the Ras-cyclic AMP pathway [46].

More alterations in phosphoproteins were found compared to proteins. An overlap of 122 out of 366 phosphoproteins (33.33%) at two or three measuring points was observed (Figs. 2G and 5D-F). These overlapping phosphoproteins include the upregulation of FTH1 [Ser-179] and STEAP3 [Ser-17, Ser-19, and/or Ser-20]. All three iron-carbohydrate complexes lead to the absence of phosphorylated residues of the macrophage mannose receptor MRC1 (IS [Ser-1105, Thr-1107, and Ser-1108], FCM [Ser-1105] and IIM [Ser-1105]). Other similar changes were observed in the phosphorylation of the BRAF kinase after treatment with IS [Ser-729 uniquely present], FCM [Ser-446 Log_2(FC) = 1.23], and IIM [Ser-729 uniquely present]. Furthermore, it is worth noting that BMP2K, which is important for clathrin-mediated endocytosis [47], was also found to be differentially regulated on phosphopeptide level with all three products (IS [Ser-1031 absent], FCM [Ser-1031 and Ser-1032 absent], and IIM [Ser-1107 and Ser-1111 uniquely present, Ser-1032 Log_2(FC) = −2.93]). In summary, our data show that the carbohydrate ligands of the iron-carbohydrate complexes have an influence on which proteins are expressed and phosphorylated in macrophages. Since the iron concentration was set at the same level in all experiments, it can be assumed that the differences are mainly driven by the nanoparticle's surface carbohydrate structures. More information on protein alterations can be found in the supplementary information (Tables S1 and S2).

4. Discussion

Iron-carbohydrate complexes are the standard of care for patients with severe iron deficiency. Their mode of action at the cellular and molecular level is currently not fully understood, especially in macrophages, which represent the main entry point of iron in the human body [48]. In this project, we used a (phospho-)proteomics approach to provide a detailed characterization and understanding of the cellular events in macrophages initiated by the treatment with these nanomedicines. By conducting a time course analysis of the treatment with iron sucrose (IS), we shed light on its cellular uptake mechanisms, usage, and transfer of the iron to intracellular storage sites in M2 macrophages (Fig. 6). In addition to the involvement of the transferrin receptor 1 (TFRC1), we propose other previously unknown receptors to play a role in the uptake of IS. Our data further suggests autophagy as a molecular stress response to high levels of intracellular iron. In parallel, a cross-sectional comparison between IS, ferric carboxymaltose (FCM), and iron isomaltoside-1000 (IIM), confirmed the importance of the structural differences on the dynamics of uptake of the different products. This is an important finding which bridges the physicochemical properties of the iron-carbohydrate complexes and their clinical outcome.

IS is an iron-carbohydrate complex with dynamic iron core-ligand kinetic properties that can release a small proportion of iron directly

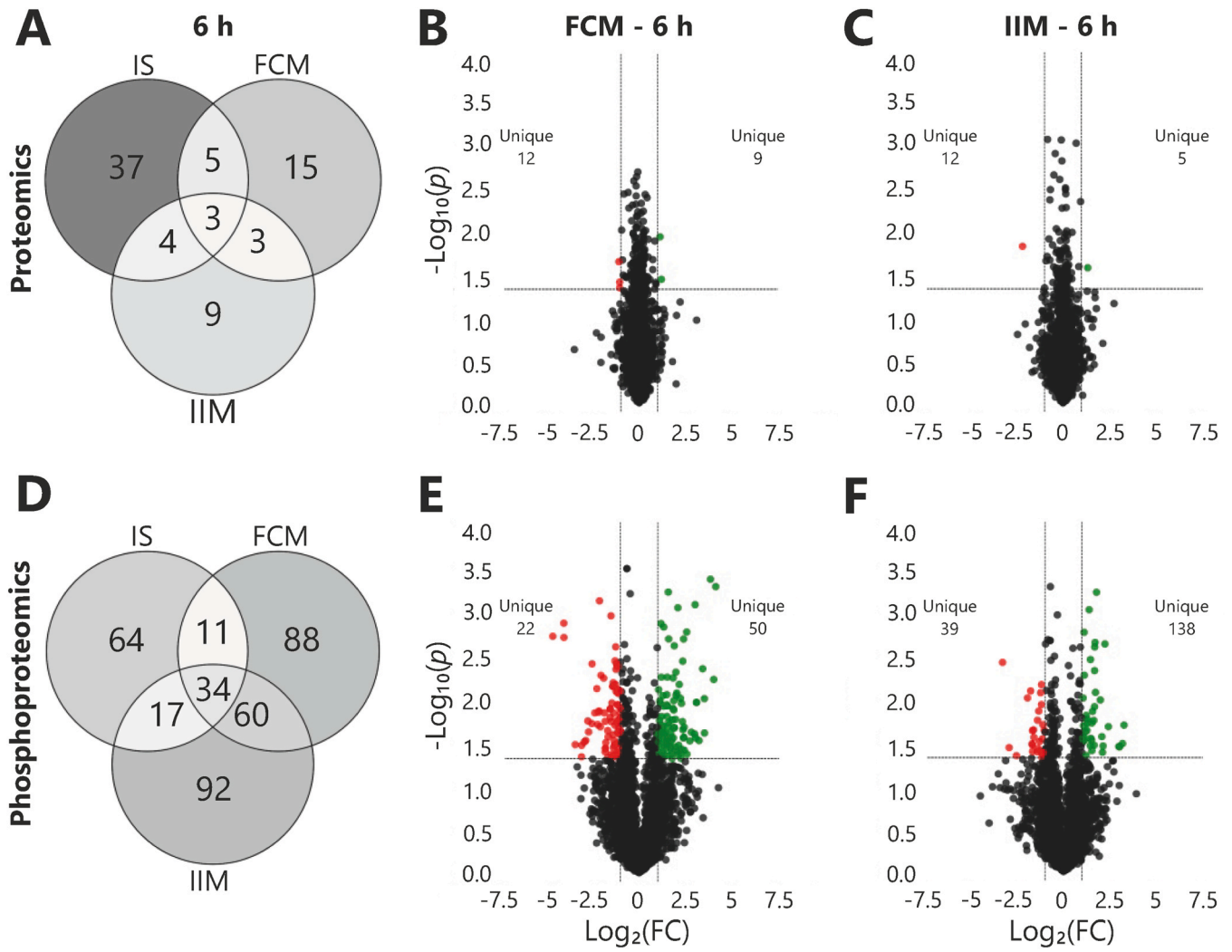

Fig. 5. Changes in M2 macrophage protein expression and phosphorylation after FCM or IIM treatment. (A) Venn diagram with the numbers of treatment-specific differentially expressed proteins and corresponding volcano plots after 6 h of (B) FCM (ferric carboxymaltose) and (C) IIM (iron isomaltoside-1000) treatment. (D) Venn diagram with the numbers of treatment-specific differentially phosphorylated proteins and corresponding volcano plots on the level of phosphopeptides after 6 h of (E) FCM and (F) IIM treatment. Colored dots represent hits with a significant p-value < 0.05 and a $|\mathrm{Log_2(FC)}| \geq 1$ when comparing FCM or IIM treated with untreated M2 macrophages. Green dots were identified to be upregulated and red dots downregulated hits compared to untreated controls.

to transferrin after intravenous administration [49]. Our results suggest that the endocytosis of TFRC1, which probably marks the best known cellular uptake mechanism of iron, plays a role in the entry mechanism of iron released from IS into M2 macrophages (as referred to in the upper central part of Fig. 6). This becomes evident due to the upregulation of a phosphopeptide of the proteins FCHO2 [S-394] ($\mathrm{Log_2(FC)} = 2.23$) and EPS15L1 [Ser-255] ($\mathrm{Log_2(FC)} = 3.23$), which are known to be required for the clathrin-mediated endocytosis of TFRC1 [50,51]. In parallel, the absence of a RAB11FIP1 [Ser-345] phosphopeptide might impair the recycling of the TFRC1 receptor [52]. Other molecular changes include phosphopeptides of the ferrireductase STEAP3 [Ser-19, Ser-20] ($\mathrm{Log_2(FC)} = 2.19$ and 2.80), a protein known to reduce Fe^{3+} to Fe^{2+} in endosomes [53], as critical factors for the transport of transferrin-derived iron via DMT1 into the cytoplasma [54]. Although the indications of reduced presence of TFRC1 on the cell surface and the induced endosomal ferrireductase suggests an involvement of TFRC1 in the uptake mechanism of iron ions dissociated from IS in M2 macrophages, our results do not imply that the TFRC1, which itself was not found to be differentially regulated, is the main or exclusive uptake mechanism of IS. Indeed, our data suggest that also complete nanoparticles enter the macrophages (right edge of Fig. 6). This notion is supported by the changes in the expression and phosphorylation of scavenging (MRC1 [55,56] [unique absence of Ser-1105, Ser-1107, Ser-1108], CD209 [57,58] ($\mathrm{Log_2(FC)} = -1.91$ and -2.08)), LDL (SCARF1 [59,60] [unique presence of Ser-606], LRP1 [61,62] [unique absence of Ser-4520], MSR1 [60] ($\mathrm{Log_2(FC)} = -1.27$ and -1.11), STAB1 [63] ($\mathrm{Log_2(FC)} = -1.13$ and -1.01)), and immunoglobulin (FCGR3A [64,65] ($\mathrm{Log_2(FC)} = -1.66$)) receptors, which bind molecules potentially found in the protein corona formed after the nanoparticles exposure to serum proteins. Our data are consistent with previous studies that attribute a higher amount of low molecular weight iron to IS compared to FCM and IIM, which is released directly upon injection, but most of the dose remains as intact nanoparticles potentially interacting with serum proteins [66]. This concept contradicts the assumption of Neu *et al.*, that iron-carbohydrate complexes are fully dissociated and exclusively taken up by cells via interaction with transferrin [67].

Our data support the notion that iron-carbohydrate complexes can be used by human macrophages as a source of iron that will eventually be stored in the cell. It is a general consensus that, upon exposure to different forms of iron (e.g. Fe-NTA and induced erythrophagocytosis), macrophages increase the expression of ferritin [68–70], which so far has not been described for IS. After 6 h of IS treatment, a significant increase in the intracellular ferritin level was detectable in our in vitro experimental setup (Fig. 3). Besides, the levels of FTH1 and FTL ferritin

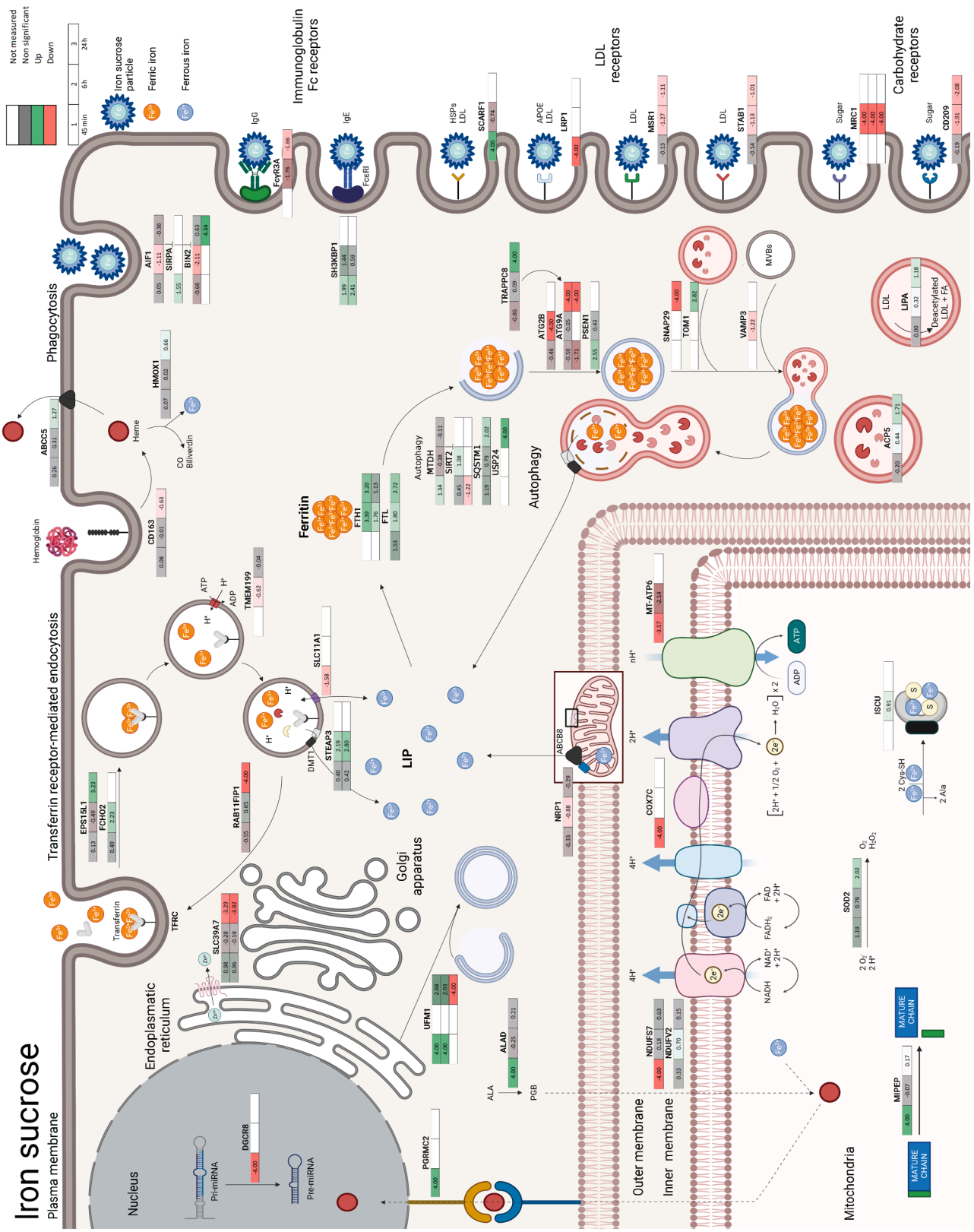

Fig. 6. Illustration of most prominent molecular changes in macrophages after IS treatment. Trend diagram with selected proteins from calculated, unique, and iron-related hits. Under each gene symbol, a row with Log_2(FC) values at the three respective time points after treatment with IS (iron sucrose) are shown per protein or phosphopeptide. The values 4.00 and − 4.00 indicate instances present uniquely in one of the conditions. Blank cells indicate that the specific protein or phosphopeptide was not measured at the given time point. A shaded cell corresponds to non-significant changes, green represents up-, and red downregulation. Protein functions were taken from the literature and manually reduced to the most interesting ones. Adapted from "Electron Transport Chain" and "Krebs Cycle", by BioRender.com (2023).

chain proteins remained high after 24 h of treatment. Our data correlates with clinical data that show a fourfold increase of serum ferritin from 6 to 24 h after IV injection of iron-carbohydrate complexes [10]. Since there is a general consensus that serum ferritin is a parameter indicative of iron storage [11,71], our observation of increased ferritin chains corresponds to the process of intracellular iron storage and ferritin release from the macrophages.

Macrophage polarization is of great interest due to its influence on the development and progression of various pathological conditions. IS has been shown to influence macrophage activation and differentiation, although the exact effects on polarization are not yet fully understood, while iron-dextran and ferumoxytol are known to favor pro-inflammatory macrophage polarization [12,13,72,73]. Similarly, our data show that IS leads to the downregulation of M2 polarization surface markers CD163 [74] ($Log_2(FC) = -0.63$), CD209 [74], and triggered the absence of three phosphphopeptides of MRC1 [75] (Fig. 6). It was observed that after 45 min of IS treatment, the cells exhibit a higher GSK3A and GSK3B activity (FDR < 0.01). These kinases are mainly linked to a suppression of the M2 polarization [76]. Simultaneously, cells exhibit a lower Akt1 activity (FDR < 0.01), which in contrast is believed to be required for M2 polarization [77]. More details on differences in kinase activities (Table S7), corresponding kinase dendograms (Figs. S2-S4), as well as upstream NP (Table S8), and PSP (Table S9) results can be found in the supplementary information. Furthermore, the identified over-representation of the term *Neutrophil degranulation* (Fig. 2I and J) indicates an altered immunological response. Overall, the observed changes are in line with studies on other iron-carbohydrate complexes [72,73], and support the hypothesis that IS can influence macrophage polarization similar to other iron-carbohydrate complexes and drive a loss of anti-inflammatory M2 activity.

Cellular iron overload has the capability to negatively influence cell survival and induce toxic effects [78]. The cytotoxic potential of labile iron is derived from the catalytic activity through the Fenton reaction enhancing the formation of hydroxyl radicals (OH˙) from hydrogen peroxide (H_2O_2) [79]. Reactive oxygen species (ROS) derived from the Fenton reaction and subsequent lipid peroxidation can lead to ferroptosis, which is an iron-dependent form of programmed cell death [80,81]. Cells can respond to the exposure to stressful stimuli (e.g. nutrient stress) with induced autophagy, a recycling pathway to clear impaired molecules and organelles [82]. It has been reported that the administration of IS induces the production of ROS and oxidative stress [83,84]. We therefore investigated how the treatment with IS nanoparticles influences proteins involved in ferroptosis and autophagy (right side of Fig. 6). We observed that in response to IS treatment, M2 macrophages initiate protective mechanisms against ferroptosis, including alterations affecting the labile iron pool (LIP), the heme metabolism and zinc transport. In the context of LIP, ATM (FDR < 0.01), an atypical kinase essential for ferroptosis [81], was downregulated after an IS treatment for 45 min. Its inhibition leads to increased expression of iron regulators involved in iron storage and export, lowering the LIP [81]. This observation is consistent with the previously discussed induced storage of iron in the form of ferritin, which itself is known to have protective effects. The protective mechanism is further supported by the downregulation of two phosphopeptides of SLC39A7 [Ser-275, Ser-276] ($Log_2(FC) = -3.29$ and -3.92). SLC39A7 is a Zn^{2+} transporter [85], and its inhibition is known to protect cells against ferroptosis [86]. Furthermore, the IS treatment affected proteins involved in the heme metabolism (CD163 [87], ABCC5 [88] [Ser-509] ($Log_2(FC) = 1.27$), HMOX1 [89,90] ($Log_2(FC) = 0.66$)). We also observed an upregulation of different proteins involved in autophagy already at 45 min of treatment (lower right part of Fig. 6). Interestingly, the upregulation of autophagy proteins was reversed after 6 h of treatment, suggesting that M2 macrophages successfully adapt to the increased iron availability by mitigating the effects of the transiently elevated LIP, in particular, the products of the Fenton reaction. Taken together, our data show that an early increase in autophagy is triggered by IS, which might be a molecular stress response to an overload of iron ions. Subsequently, the macrophages show successful cellular adaptation, which is reflected by a downregulation of autophagy and the described possible reduction of the LIP, preventing ferroptosis.

The surface characteristics of the iron-carbohydrate complexes can have an influence on their PK/PD profiles [5]. In the clinical setting, it has been observed that IS is cleared faster from the plasma than other products that have more stable coordinative bonds, like FCM and IIM [5,10]. In the present study, the response of M2 macrophages to IS, FCM, and IIM treatments was compared in a cross-sectional manner (6 h treatment with a clinical dose, corresponding to 1800 μM of total iron). A 6 h time point allows for comparison of the initial response of macrophages to the different iron products [10]. Our results suggest that iron-carbohydrate complexes with a longer serum half-life (FCM and IIM) tend to be taken up and transfer bioavailable iron to intracellular ferritin at a slower rate than IS. The number of proteomic changes (Fig. 5A) inversely correlated with the serum half-life of the IV iron-carbohydrate complexes (IS < FCM < IIM) reported in the literature [10]. Our data show that some (phospho-)proteins like FTH1, FTL, STEAP3, and MRC1 that are highly altered (up- or downregulated) by IS, are also modified by FCM and IIM but to a lesser extent. Furthermore, IIM induced the phosphorylation of a RAB11FIP1 [Ser-206] residue, indicating that the cells are still keen to take up additional transferrin via the TFRC1 after 6 h of treatment. Although our data imply slower but similar uptake mechanisms between products, variations in protein expression and phosphorylation patterns highlight complex and specific differences that are likely driven by the individual nanoparticle's physical properties, such as surface characteristics versus the polynuclear iron core. With regard to macrophage polarization, our results demonstrate a loss of the M2 polarization activity with lower carbohydrate ligand stabilities (IS < FCM < IIM). Although FCM and IIM also triggered the downregulation of an MRC1 phosphopeptide (M2 marker), changes in kinase activities are not fully supportive of the loss of anti-inflammatory responses. In this regard, FCM and IIM lead to the upregulation of Akt1 and CK2A1 (Figs. S5 and S6), a catalytic subunit of CK2 known to phosphorylate and activate Akt1 itself [91], essentially the opposite of IS at an earlier time point (45 min). Additionally, FCM upregulated the M2 suppressing GSK3B kinase (Fig. S5). Since some studies have attributed a critical role to iron and iron-carbohydrate complexes in shaping macrophage polarization [72,73,92], it can be speculated that the different complexed iron-carbohydrates influence the triggered molecular changes related to cell polarization.

It should be noted that the observations of this study are based on large-scale proteomics and phosphoproteomics analyses providing novel insights regarding how iron-carbohydrate complexes interact with macrophages and how the iron is made available to the bone marrow and finally achieving a therapeutic benefit. Although we experimentally confirmed the increase of iron content induced by the treatment with IS, FCM, and IIM in primary human M2 macrophages with ICP-OES, further experimental approaches using more advanced systems (e.g. whole blood, co-culture with hepatocytes, dynamic perfusion model) could be used to confirm the biorelevance of the identified molecular mechanism. In addition to other technical approaches to quantify different forms of iron species (e.g. Fe^{3+} ions, Fe^{2+} ions, iron nanoparticles) iron influx and efflux patterns can be evaluated to discriminate the contribution on the global biological impact of the iron-carbohydrate complexes, which is beyond the focus of this study.

In conclusion, our findings contribute to the molecular level understanding of the uptake, biodegradation and metabolic processing of iron-carbohydrate complexes in macrophages. Insights gleaned from this study can serve as basis for linking the physicochemical properties of iron-carbohydrates with their clinical outcome. Despite being used for many decades for clinical treatment, there are still significant research gaps regarding the uptake and intracellular processing of iron-carbohydrate complexes. Advancing the understanding of these

fundamental biologic interactions will allow for greater correlation of physicochemical characteristics with in vivo behavior of these widely used nanomedicines. Additionally, understanding the various intracellular pathways involved with the bioprocessing of iron-carbohydrate nanomedicines will facilitate future computational models that could support regulatory science initiatives. Importantly, our untargeted (phospho-)proteomics approach provides global and novel insights into intracellular changes in the levels of protein expression and phosphorylation influenced by these widely used products. These types of omics and multi-omics approaches have the potential to innovate mechanistic studies for complex drugs.

Funding

This work was financed by CSL-Vifor.

CRediT authorship contribution statement

Jonas Bossart: Software, Formal analysis, Investigation, Data curation, Writing – original draft, Visualization, Project administration. **Alexandra Rippl:** Investigation, Writing – review & editing. **Marija Buljan:** Validation, Writing – review & editing, Supervision. **Amy E. Barton Alston:** Writing – review & editing. **Beat Flühmann:** Writing – review & editing. **Reinaldo Digigow:** Writing – review & editing. **Vanesa Ayala-Nunez:** Conceptualization, Investigation, Writing – original draft, Supervision, Project administration, Funding acquisition. **Peter Wick:** Conceptualization, Writing – review & editing, Supervision, Funding acquisition.

Declaration of Competing Interest

The authors declare the following financial interests/personal relationships which may be considered as potential competing interests: Amy E. Barton Alston, Beat Flühmann, and Reinaldo Digigow are employees of CSL-Vifor. This work was financed by CSL-Vifor.

Data availability

MaxQuant output data are available as a merged excel file in the supplementary data (Table S10). The raw MS data will be made available upon reasonable request by email to jonas.bossart@empa.ch.

Acknowledgments

We would like to express our gratitude to the members of the FGCZ for technical assistance, measurements, and discussions.

Appendix A. Supporting information

Supplementary data associated with this article can be found in the online version at doi:10.1016/j.biopha.2023.115404.

References

[1] T. Richards, C. Breymann, M.J. Brookes, S. Lindgren, I.C. Macdougall, L. P. McMahon, M.G. Munro, E. Nemeth, G.M.C. Rosano, I. Schiefke, G. Weiss, Questions and answers on iron deficiency treatment selection and the use of intravenous iron in routine clinical practice, Ann. Med. 53 (2021) 274–285, https://doi.org/10.1080/07853890.2020.1867323.

[2] P. Geisser, S. Burckhardt, The pharmacokinetics and pharmacodynamics of iron preparations, Pharmaceutics 3 (2011) 12–33, https://doi.org/10.3390/pharmaceutics3010012.

[3] J.N. Nanas, C. Matsouka, D. Karageorgopoulos, A. Leonti, E. Tsolakis, S.G. Drakos, E.P. Tsagalou, G.D. Maroulidis, G.P. Alexopoulos, J.E. Kanakakis, M.I. Anastasiou-Nana, Etiology of anemia in patients with advanced heart failure, J. Am. Coll. Cardiol. 48 (2006) 2485–2489, https://doi.org/10.1016/j.jacc.2006.08.034.

[4] C. Gasche, M.C.E. Lomer, I. Cavill, G. Weiss, Iron, anaemia, and inflammatory bowel diseases, Gut 53 (2004) 1190–1197, https://doi.org/10.1136/gut.2003.035758.

[5] F. Funk, B. Flühmann, A.E. Barton, Criticality of surface characteristics of intravenous iron–carbohydrate nanoparticle complexes: implications for pharmacokinetics and pharmacodynamics, Int. J. Mol. Sci. 23 (2022) 2140, https://doi.org/10.3390/ijms23042140.

[6] P.A. Kalra, S. Bhandari, Efficacy and safety of iron isomaltoside (Monofer®) in the management of patients with iron deficiency anemia, Int. J. Nephrol. Renov. Dis. 9 (2016) 53–64, https://doi.org/10.2147/IJNRD.S89704.

[7] F. Vanobberghen, O. Lweno, A. Kuemmerle, K.D. Mwebi, P. Asilia, A. Issa, B. Simon, S. Mswata, S. Schmidlin, T.R. Glass, S. Abdulla, C. Daubenberger, M. Tanner, S. Meyer-Monard, Efficacy and safety of intravenous ferric carboxymaltose compared with oral iron for the treatment of iron deficiency anaemia in women after childbirth in Tanzania: a parallel-group, open-label, randomised controlled phase 3 trial, Lancet Glob. Health 9 (2021) e189–e198, https://doi.org/10.1016/S2214-109X(20)30448-4.

[8] G. Bansal, J. Burton, N. Yee Win, S. Selahi, S. Foss, Assessment of the Efficacy of Intravenous Iron Therapy (Venofer®) in the Treatment of Iron Deficiency Anemia (IDA), Blood 116 (2010) 4229, https://doi.org/10.1182/blood.V116.21.4229.4229.

[9] S. Beshara, H. Lundqvist, J. Sundin, M. Lubberink, V. Tolmachev, S. Valind, G. Antoni, B. Långström, B.G. Danielson, Pharmacokinetics and red cell utilization of iron(III) hydroxide–sucrose complex in anaemic patients: a study using positron emission tomography, Br. J. Haematol. 104 (1999) 296–302, https://doi.org/10.1046/j.1365-2141.1999.01179.x.

[10] M.W. Garbowski, S. Bansal, J.B. Porter, C. Mori, S. Burckhardt, R.C. Hider, Intravenous iron preparations transiently generate non-transferrin-bound iron from two proposed pathways, 0–0, Haematologica (2020), https://doi.org/10.3324/haematol.2020.250803.

[11] T. Arsiwala, A.-C.S. Vogt, A.E. Barton, V. Manolova, F. Funk, B. Flühmann, M. F. Bachmann, Kupffer Cells and Blood Monocytes Orchestrate the Clearance of Iron–Carbohydrate Nanoparticles from Serum, Int. J. Mol. Sci. 23 (2022) 2666, https://doi.org/10.3390/ijms23052666.

[12] H. Ichii, Y. Masuda, T. Hassanzadeh, M. Saffarian, S. Gollapudi, N.D. Vaziri, Iron sucrose impairs phagocytic function and promotes apoptosis in polymorphonuclear leukocytes, Am. J. Nephrol. 36 (2012) 50–57, https://doi.org/10.1159/000339285.

[13] L.H. Fell, S. Seiler-Mußler, A.B. Sellier, B. Rotter, P. Winter, M. Sester, D. Fliser, G. H. Heine, A.M. Zawada, Impact of individual intravenous iron preparations on the differentiation of monocytes towards macrophages and dendritic cells, Nephrol. Dial. Transplant. 31 (2016) 1835–1845, https://doi.org/10.1093/ndt/gfw045.

[14] M.R. Jahn, H.B. Andreasen, S. Fütterer, T. Nawroth, V. Schünemann, U. Kolb, W. Hofmeister, M. Muñoz, K. Bock, M. Meldal, P. Langguth, A comparative study of the physicochemical properties of iron isomaltoside 1000 (Monofer®), a new intravenous iron preparation and its clinical implications, Eur. J. Pharm. Biopharm. 78 (2011) 480–491, https://doi.org/10.1016/j.ejpb.2011.03.016.

[15] I. Blumenstein, S. Shanbhag, P. Langguth, P.A. Kalra, H. Zoller, W. Lim, Newer formulations of intravenous iron: a review of their chemistry and key safety aspects – hypersensitivity, hypophosphatemia, and cardiovascular safety, Expert Opin. Drug Saf. 20 (2021) 757–769, https://doi.org/10.1080/14740338.2021.1912010.

[16] M. Praschberger, C. Cornelius, M. Schitegg, H. Goldenberg, B. Scheiber-Mojdehkar, B. Sturm, Bioavailability and stability of intravenous iron sucrose originator versus generic iron sucrose AZAD, Pharm. Dev. Technol. 20 (2015) 176–182, https://doi.org/10.3109/10837450.2013.852575.

[17] T. Moos, K. Møllgård, A sensitive post-DAB enhancement technique for demonstration of iron in the central nervous system, Histochemistry 99 (1993) 471–475, https://doi.org/10.1007/BF00274100.

[18] C.S. Hughes, S. Foehr, D.A. Garfield, E.E. Furlong, L.M. Steinmetz, J. Krijgsveld, Ultrasensitive proteome analysis using paramagnetic bead technology, Mol. Syst. Biol. 10 (2014) 757, https://doi.org/10.15252/msb.20145625.

[19] M. Leutert, R.A. Rodríguez-Mias, N.K. Fukuda, J. Villén, R2–P2 rapid-robotic phosphoproteomics enables multidimensional cell signaling studies, Mol. Syst. Biol. 15 (2019), https://doi.org/10.15252/msb.20199021.

[20] C. Türker, F. Akal, D. Joho, C. Panse, S. Barkow-Oesterreicher, H. Rehrauer, R. Schlapbach, B-Fabric: the Swiss Army Knife for life sciences, in: B-Fabric: the Swiss Army Knife for life sciences, EDBT, ACM Press, Lausanne, Switzerland, 2010, https://doi.org/10.1145/1739041.1739135.

[21] J. Cox, M. Mann, MaxQuant enables high peptide identification rates, individualized p.p.b.-range mass accuracies and proteome-wide protein quantification, Nat. Biotechnol. 26 (2008) 1367–1372, https://doi.org/10.1038/nbt.1511.

[22] The UniProt Consortiu, UniProt: the universal protein knowledgebase in 2021, Nucleic Acids Res 49 (2020) D480–D489, https://doi.org/10.1093/nar/gkaa1100.

[23] T. Kluyver, B. Ragan-Kelly, F. Pérez, B. Granger, M. Bussonnier, J. Frederic, K. Kelley, J. Hamrick, J. Grout, S. Corlay, P. Ivanov, D. Avila, S. Abdalla, C. Willing, Jupyter Notebooks—a publishing format for reproducible computational workflows, in: Position. Power Acad. Publ. Play. Agents Agendas, IOS Press, Netherlands, 2016, https://doi.org/10.3233/978-1-61499-649-1-87.

[24] S. Tyanova, T. Temu, J. Cox, The MaxQuant computational platform for mass spectrometry-based shotgun proteomics, Nat. Protoc. 11 (2016) 2301–2319, https://doi.org/10.1038/nprot.2016.136.

[25] G. Van Rossum, F.L. Drake, Python 3 Reference Manual, CreateSpace, Scotts Valley, CA, 2009.

[26] A. Ressa, M. Fitzpatrick, H. van den Toorn, A.J.R. Heck, M. Altelaar, PaDuA: A Python Library for High-Throughput (Phospho)proteomics Data Analysis, J. Proteome Res 18 (2019) 576–584, https://doi.org/10.1021/acs.jproteome.8b00576.

[27] The Pandas Development Team, pandas-dev/pandas: Pandas, 2022. ⟨https://doi.org/10.5281/ZENODO.3509134⟩.
[28] C.R. Harris, K.J. Millman, S.J. van der Walt, R. Gommers, P. Virtanen, D. Cournapeau, E. Wieser, J. Taylor, S. Berg, N.J. Smith, R. Kern, M. Picus, S. Hoyer, M.H. van Kerkwijk, M. Brett, A. Haldane, J.F. del Río, M. Wiebe, P. Peterson, P. Gérard-Marchant, K. Sheppard, T. Reddy, W. Weckesser, H. Abbasi, C. Gohlke, T.E. Oliphant, Array programming with NumPy, Nature 585 (2020) 357–362, https://doi.org/10.1038/s41586-020-2649-2.
[29] P. Virtanen, R. Gommers, T.E. Oliphant, M. Haberland, T. Reddy, D. Cournapeau, E. Burovski, P. Peterson, W. Weckesser, J. Bright, S.J. van der Walt, M. Brett, J. Wilson, K.J. Millman, N. Mayorov, A.R.J. Nelson, E. Jones, R. Kern, E. Larson, C. J. Carey, İ. Polat, Y. Feng, E.W. Moore, J. VanderPlas, D. Laxalde, J. Perktold, R. Cimrman, I. Henriksen, E.A. Quintero, C.R. Harris, A.M. Archibald, A.H. Ribeiro, F. Pedregosa, P. van Mulbregt, SciPy 1.0: fundamental algorithms for scientific computing in Python, Nat. Methods 17 (2020) 261–272, https://doi.org/10.1038/s41592-019-0686-2.
[30] J.D. Hunter, Matplotlib: A 2D Graphics Environment, Comput. Sci. Eng. 9 (2007) 90–95, https://doi.org/10.1109/MCSE.2007.55.
[31] J.C. Oliveros, Venny. An interactive tool for comparing lists with Venn's diagrams., 2007. ⟨https://bioinfogp.cnb.csic.es/tools/venny/index.html⟩.
[32] R. Herwig, C. Hardt, M. Lienhard, A. Kamburov, Analyzing and interpreting genome data at the network level with ConsensusPathDB, Nat. Protoc. 11 (2016) 1889–1907, https://doi.org/10.1038/nprot.2016.117.
[33] J. Griss, G. Viteri, K. Sidiropoulos, V. Nguyen, A. Fabregat, H. Hermjakob, ReactomeGSA - Efficient Multi-Omics Comparative Pathway Analysis, Mol. Cell. Proteom. MCP 19 (2020) 2115–2124, https://doi.org/10.1074/mcp.TIR120.002155.
[34] M. Kanehisa, S. Goto, KEGG: kyoto encyclopedia of genes and genomes, Nucleic Acids Res 28 (2000) 27–30, https://doi.org/10.1093/nar/28.1.27.
[35] D.W. Huang, B.T. Sherman, R.A. Lempicki, Systematic and integrative analysis of large gene lists using DAVID bioinformatics resources, Nat. Protoc. 4 (2009) 44–57, https://doi.org/10.1038/nprot.2008.211.
[36] Y. Benjamini, Y. Hochberg, Controlling the false discovery rate: a practical and powerful approach to multiple testing, J. R. Stat. Soc. Ser. B Method. 57 (1995) 289–300.
[37] P.V. Hornbeck, J.M. Kornhauser, S. Tkachev, B. Zhang, E. Skrzypek, B. Murray, V. Latham, M. Sullivan, PhosphoSitePlus: a comprehensive resource for investigating the structure and function of experimentally determined post-translational modifications in man and mouse, Nucleic Acids Res 40 (2012) D261–D270, https://doi.org/10.1093/nar/gkr1122.
[38] H. Horn, E.M. Schoof, J. Kim, X. Robin, M.L. Miller, F. Diella, A. Palma, G. Cesareni, L.J. Jensen, R. Linding, KinomeXplorer: an integrated platform for kinome biology studies, Nat. Methods 11 (2014) 603–604, https://doi.org/10.1038/nmeth.2968.
[39] A. Gramfort, M. Luessi, E. Larson, D. Engemann, D. Strohmeier, C. Brodbeck, R. Goj, M. Jas, T. Brooks, L. Parkkonen, M. Hämäläinen, MEG and EEG data analysis with MNE-Python, Front. Neurosci. 7 (2013), https://doi.org/10.3389/fnins.2013.00267.
[40] K.S. Metz, E.M. Deoudes, M.E. Berginski, I. Jimenez-Ruiz, B.A. Aksoy, J. Hammerbacher, S.M. Gomez, D.H. Phanstiel, Coral: Clear and customizable visualization of human kinome data, e1, Cell Syst. 7 (2018) 347–350, https://doi.org/10.1016/j.cels.2018.07.001.
[41] J. Hoppstädter, M. Seif, A. Dembek, C. Cavelius, H. Huwer, A. Kraegeloh, A. K. Kiemer, M2 polarization enhances silica nanoparticle uptake by macrophages, Front. Pharmacol. 6 (2015), https://doi.org/10.3389/fphar.2015.00055.
[42] K.A. Binnemars-Postma, H.W. ten Hoopen, G. Storm, J. Prakash, Differential uptake of nanoparticles by human M1 and M2 polarized macrophages: protein corona as a critical determinant, Nanomed 11 (2016) 2889–2902, https://doi.org/10.2217/nnm-2016-0233.
[43] D.R. Jayaram, S. Frost, C. Argov, V.B. Liju, N.P. Anto, A. Muraleedharan, A. Ben-Ari, R. Sinay, I. Smoly, O. Novoplansky, N. Isakov, D. Toiber, C. Keasar, M. Elkabets, E. Yeger-Lotem, E. Livneh, Unraveling the hidden role of a uORF-encoded peptide as a kinase inhibitor of PKCs, Proc. Natl. Acad. Sci. U. S. A 118 (2021), e2018899118, https://doi.org/10.1073/pnas.2018899118.
[44] A. Lykidis, P.D. Jackson, C.O. Rock, S. Jackowski, The Role of CDP-Diacylglycerol Synthetase and Phosphatidylinositol Synthase Activity Levels in the Regulation of Cellular Phosphatidylinositol Content*, J. Biol. Chem. 272 (1997) 33402–33409, https://doi.org/10.1074/jbc.272.52.33402.
[45] P.K. Ehrenberg, S. Shangguan, B. Issac, G. Alter, A. Geretz, T. Izumi, C. Bryant, M. A. Eller, F. Wegmann, R. Apps, M. Creegan, D.L. Bolton, R.P. Sekaly, M.L. Robb, R. A. Gramzinski, M.G. Pau, H. Schuitemaker, D.H. Barouch, N.L. Michael, R. Thomas, A vaccine-induced gene expression signature correlates with protection against SIV and HIV in multiple trials, Sci. Transl. Med. 11 (2019), eaaw4236, https://doi.org/10.1126/scitranslmed.aaw4236.
[46] Y. Pan, J.H.M. Tong, R.W.M. Lung, W. Kang, J.S.H. Kwan, W.P. Chak, K.Y. Tin, L. Y. Chung, F. Wu, S.S.M. Ng, T.W.C. Mak, J. Yu, K.W. Lo, A.W.H. Chan, K.F. To, RASAL2 promotes tumor progression through LATS2/YAP1 axis of hippo signaling pathway in colorectal cancer, Mol. Cancer 17 (2018) 102, https://doi.org/10.1186/s12943-018-0853-6.
[47] S.T. Ramesh, K.V. Navyasree, S. Sah, A.B. Ashok, N. Qathoon, S. Mohanty, R. K. Swain, P.K. Umasankar, BMP2K phosphorylates AP-2 and regulates clathrin-mediated endocytosis, Traffic 22 (2021) 377–396, https://doi.org/10.1111/tra.12814.
[48] A. Barton Alston, R. Digigow, B. Flühmann, M.G. Wacker, Putting square pegs in round holes: Why traditional pharmacokinetic principles cannot universally be applied to iron-carbohydrate complexes, Eur. J. Pharm. Biopharm. 188 (2023) 6–14, https://doi.org/10.1016/j.ejpb.2023.04.025.
[49] F. Funk, P. Ryle, C. Canclini, S. Neiser, P. Geisser, The new generation of intravenous iron: chemistry, pharmacology, and toxicology of ferric carboxymaltose, Arzneimittelforschung 60 (2011) 345–353, https://doi.org/10.1055/s-0031-1296299.
[50] A. Uezu, K. Umeda, K. Tsujita, S. Suetsugu, T. Takenawa, H. Nakanishi, Characterization of the EFC/F-BAR domain protein, FCHO2, Genes Cells 16 (2011) 868–878, https://doi.org/10.1111/j.1365-2443.2011.01536.x.
[51] C. Milesi, P. Alberici, B. Pozzi, A. Oldani, G.V. Beznoussenko, A. Raimondi, B. E. Soppo, S. Amodio, G. Caldieri, M.G. Malabarba, G. Bertalot, S. Confalonieri, D. Parazzoli, A.A. Mironov, C. Tacchetti, P.P. Di Fiore, S. Sigismund, N. Offenhäuser, Redundant and nonredundant organismal functions of EPS15 and EPS15L1, Life Sci. Alliance 2 (2019), e201800273, https://doi.org/10.26508/lsa.201800273.
[52] A.A. Peden, E. Schonteich, J. Chun, J.R. Junutula, R.H. Scheller, R. Prekeris, The RCP–Rab11 Complex Regulates Endocytic Protein Sorting, Mol. Biol. Cell. 15 (2004) 3530–3541, https://doi.org/10.1091/mbc.e03-12-0918.
[53] R.S. Ohgami, D.R. Campagna, E.L. Greer, B. Antiochos, A. McDonald, J. Chen, J. J. Sharp, Y. Fujiwara, J.E. Barker, M.D. Fleming, Identification of a ferrireductase required for efficient transferrin-dependent iron uptake in erythroid cells, Nat. Genet. 37 (2005) 1264–1269, https://doi.org/10.1038/ng1658.
[54] M.D. Fleming, C.C. Trenor, M.A. Su, D. Foernzler, D.R. Beier, W.F. Dietrich, N. C. Andrews, Microcytic anaemia mice have a mutation in Nramp2, a candidate iron transporter gene, Nat. Genet. 16 (1997) 383–386, https://doi.org/10.1038/ng0897-383.
[55] Y. Su, T. Bakker, J. Harris, C. Tsang, G.D. Brown, M.R. Wormald, S. Gordon, R. A. Dwek, P.M. Rudd, L. Martinez-Pomares, Glycosylation Influences the Lectin Activities of the Macrophage Mannose Receptor*, J. Biol. Chem. 280 (2005) 32811–32820, https://doi.org/10.1074/jbc.M503457200.
[56] U. Gazi, L. Martinez-Pomares, Influence of the mannose receptor in host immune responses, Immunobiology 214 (2009) 554–561, https://doi.org/10.1016/j.imbio.2008.11.004.
[57] E.P. McGreal, J.L. Miller, S. Gordon, Ligand recognition by antigen-presenting cell C-type lectin receptors, Curr. Opin. Immunol. 17 (2005) 18–24, https://doi.org/10.1016/j.coi.2004.12.001.
[58] D. Montoya, D. Cruz, R.M.B. Teles, D.J. Lee, M.T. Ochoa, S.R. Krutzik, R. Chun, M. Schenk, X. Zhang, B.G. Ferguson, A.E. Burdick, E.N. Sarno, T.H. Rea, M. Hewison, J.S. Adams, G. Cheng, R.L. Modlin, Divergence of Macrophage Phagocytic and Antimicrobial Programs in Leprosy, Cell Host Microbe 6 (2009) 343–353, https://doi.org/10.1016/j.chom.2009.09.002.
[59] A. Murshid, T.J. Borges, C. Bonorino, B.J. Lang, S.K. Calderwood, Immunological Outcomes Mediated Upon Binding of Heat Shock Proteins to Scavenger Receptors SCARF1 and LOX-1, and Endocytosis by Mononuclear Phagocytes, Front. Immunol. 10 (2020) 3035, https://doi.org/10.3389/fimmu.2019.03035.
[60] H. Adachi, M. Tsujimoto, H. Arai, K. Inoue, Expression cloning of a novel scavenger receptor from human endothelial cells*, J. Biol. Chem. 272 (1997) 31217–31220, https://doi.org/10.1074/jbc.272.50.31217.
[61] M.S. Brown, J.L. Goldstein, A receptor-mediated pathway for cholesterol homeostasis, Science 232 (1986) 34–47, https://doi.org/10.1126/science.3513311.
[62] U. Beisiegel, W. Weber, G. Ihrke, J. Herz, K.K. Stanley, The LDL–receptor–related protein, LRP, is an apolipoprotein E-binding protein, Nature 341 (1989) 162–164, https://doi.org/10.1038/341162a0.
[63] H. Adachi, M. Tsujimoto, FEEL-1, a Novel Scavenger Receptor with in Vitro Bacteria-binding and Angiogenesis-modulating Activities*, J. Biol. Chem. 277 (2002) 34264–34270, https://doi.org/10.1074/jbc.M204277200.
[64] L. Coënon, M. Villalba, From CD16a biology to antibody-dependent cell-mediated cytotoxicity improvement, Front. Immunol. 13 (2022), https://doi.org/10.3389/fimmu.2022.913215.
[65] C.J. Fitzer-Attas, M. Lowry, M.T. Crowley, A.J. Finn, F. Meng, A.L. DeFranco, C. A. Lowell, Fcγ Receptor–Mediated Phagocytosis in Macrophages Lacking the Src Family Tyrosine Kinases Hck, Fgr, and Lyn, J. Exp. Med 191 (2000) 669–682, https://doi.org/10.1084/jem.191.4.669.
[66] P. Zou, K. Tyner, A. Raw, S. Lee, Physicochemical Characterization of Iron Carbohydrate Colloid Drug Products, AAPS J. 19 (2017) 1359–1376, https://doi.org/10.1208/s12248-017-0126-0.
[67] H.M. Neu, S.A. Alexishin, J.E.P. Brandis, A.M.C. Williams, W. Li, D. Sun, N. Zheng, W. Jiang, A. Zimrin, J.C. Fink, J.E. Polli, M.A. Kane, S.L.J. Michel, Snapshots of Iron Speciation: Tracking the Fate of Iron Nanoparticle Drugs via a Liquid Chromatography–Inductively Coupled Plasma–Mass Spectrometric Approach, Mol. Pharm. 16 (2019) 1272–1281, https://doi.org/10.1021/acs.molpharmaceut.8b01215.
[68] M.D. Knutson, M.R. Vafa, D.J. Haile, M. Wessling-Resnick, Iron loading and erythrophagocytosis increase ferroportin 1 (FPN1) expression in J774 macrophages, Blood 102 (2003) 4191–4197, https://doi.org/10.1182/blood-2003-04-1250.
[69] C. Delaby, N. Pilard, G. Hetet, F. Driss, B. Grandchamp, C. Beaumont, F. Canonne-Hergaux, A physiological model to study iron recycling in macrophages, Exp. Cell Res. 310 (2005) 43–53, https://doi.org/10.1016/j.yexcr.2005.07.002.
[70] M.J. Leimberg, E. Prus, A.M. Konijn, E. Fibach, Macrophages function as a ferritin iron source for cultured human erythroid precursors, J. Cell. Biochem 103 (2008) 1211–1218, https://doi.org/10.1002/jcb.21499.
[71] L.A. Cohen, L. Gutierrez, A. Weiss, Y. Leichtmann-Bardoogo, D. Zhang, D. R. Crooks, R. Sougrat, A. Morgenstern, B. Galy, M.W. Hentze, F.J. Lazaro, T. A. Rouault, E.G. Meyron-Holtz, Serum ferritin is derived primarily from

macrophages through a nonclassical secretory pathway, Blood 116 (2010) 1574–1584, https://doi.org/10.1182/blood-2009-11-253815.
[72] A. Kroner, A.D. Greenhalgh, J.G. Zarruk, R. Passos dos Santos, M. Gaestel, S. David, TNF and Increased Intracellular Iron Alter Macrophage Polarization to a Detrimental M1 Phenotype in the Injured Spinal Cord, Neuron 83 (2014) 1098–1116, https://doi.org/10.1016/j.neuron.2014.07.027.
[73] S. Zanganeh, G. Hutter, R. Spitler, O. Lenkov, M. Mahmoudi, A. Shaw, J. S. Pajarinen, H. Nejadnik, S. Goodman, M. Moseley, L.M. Coussens, H.E. Daldrup-Link, Iron oxide nanoparticles inhibit tumour growth by inducing pro-inflammatory macrophage polarization in tumour tissues, Nat. Nanotechnol. 11 (2016) 986–994, https://doi.org/10.1038/nnano.2016.168.
[74] Y. Wang, K. Yan, J. Wang, J. Lin, J. Bi, M2 Macrophage Co-Expression Factors Correlate With Immune Phenotype and Predict Prognosis of Bladder Cancer, Front. Oncol. 11 (2021), https://doi.org/10.3389/fonc.2021.609334.
[75] F.O. Martinez, S. Gordon, M. Locati, A. Mantovani, Transcriptional profiling of the human monocyte-to-macrophage differentiation and polarization: new molecules and patterns of gene expression, J. Immunol. 177 (2006) 7303–7311, https://doi.org/10.4049/jimmunol.177.10.7303.
[76] S. Patel, G. Werstuck, Characterizing the Role of Glycogen Synthase Kinase-3α/β in Macrophage Polarization and the Regulation of Pro-Atherogenic Pathways in Cultured Ldlr-/- Macrophages, Front. Immunol. 12 (2021), https://doi.org/10.3389/fimmu.2021.676752.
[77] A.C. Labonte, A.-C. Tosello-Trampont, Y.S. Hahn, The Role of Macrophage Polarization in Infectious and Inflammatory Diseases, Mol. Cells 37 (2014) 275–285, https://doi.org/10.14348/molcells.2014.2374.
[78] H. Lv, P. Shang, The significance, trafficking and determination of labile iron in cytosol, mitochondria and lysosomes, Metallomics 10 (2018) 899–916, https://doi.org/10.1039/c8mt00048d.
[79] C.C. Winterbourn, Toxicity of iron and hydrogen peroxide: the Fenton reaction, Toxicol. Lett. 82– 83 (1995) 969–974, https://doi.org/10.1016/0378-4274(95)03532-X.
[80] F. Kuang, J. Liu, D. Tang, R. Kang, Oxidative damage and antioxidant defense in ferroptosis, Front. Cell Dev. Biol. 8 (2020), https://doi.org/10.3389/fcell.2020.586578.
[81] P.-H. Chen, J. Wu, C.-K.C. Ding, C.-C. Lin, S. Pan, N. Bossa, Y. Xu, W.-H. Yang, B. Mathey-Prevot, J.-T. Chi, Kinome screen of ferroptosis reveals a novel role of ATM in regulating iron metabolism, Cell Death Differ. 27 (2020) 1008–1022, https://doi.org/10.1038/s41418-019-0393-7.
[82] D. Glick, S. Barth, K.F. Macleod, Autophagy: cellular and molecular mechanisms, J. Pathol. 221 (2010) 3–12, https://doi.org/10.1002/path.2697.
[83] J.E. Toblli, G. Cao, L. Oliveri, M. Angerosa, Comparison of Oxidative Stress and Inflammation Induced by Different Intravenous Iron Sucrose Similar Preparations in a Rat Model, Inflamm. Allergy Drug Targets 11 (2012) 66–78, https://doi.org/10.2174/187152812798889358.
[84] A. Martin-Malo, A. Merino, J. Carracedo, M.A. Alvarez-Lara, R. Ojeda, S. Soriano, R. Crespo, R. Ramirez, P. Aljama, Effects of intravenous iron on mononuclear cells during the haemodialysis session, Nephrol. Dial. Transplant. 27 (2012) 2465–2471, https://doi.org/10.1093/ndt/gfr711.
[85] K.M. Taylor, H.E. Morgan, A. Johnson, R.I. Nicholson, Structure-function analysis of HKE4, a member of the new LIV-1 subfamily of zinc transporters, Biochem. J. 377 (2004) 131–139, https://doi.org/10.1042/bj20031183.
[86] P.-H. Chen, J. Wu, Y. Xu, C.-K.C. Ding, A.A. Mestre, C.-C. Lin, W.-H. Yang, J.-T. Chi, Zinc transporter ZIP7 is a novel determinant of ferroptosis, Cell Death Dis. 12 (2021) 198, https://doi.org/10.1038/s41419-021-03482-5.
[87] M. Kristiansen, J.H. Graversen, C. Jacobsen, O. Sonne, H.-J. Hoffman, S.K.A. Law, S.K. Moestrup, Identification of the haemoglobin scavenger receptor, Nature 409 (2001) 198–201, https://doi.org/10.1038/35051594.
[88] T. Korolnek, J. Zhang, S. Beardsley, G.L. Scheffer, I. Hamza, Control of Metazoan Heme Homeostasis by a Conserved Multidrug Resistance Protein, Cell Metab. 19 (2014) 1008–1019, https://doi.org/10.1016/j.cmet.2014.03.030.
[89] X. Chen, C. Yu, R. Kang, D. Tang, Iron metabolism in ferroptosis, Front. Cell Dev. Biol. 8 (2020), https://doi.org/10.3389/fcell.2020.590226.
[90] D. Morse, A.M.K. Choi, Heme Oxygenase-1, Am. J. Respir. Cell Mol. Biol. 27 (2002) 8–16, https://doi.org/10.1165/ajrcmb.27.1.4862.
[91] C. Borgo, C. D'Amore, S. Sarno, M. Salvi, M. Ruzzene, Protein kinase CK2: a potential therapeutic target for diverse human diseases, Signal Transduct. Target. Ther. 6 (2021) 1–20, https://doi.org/10.1038/s41392-021-00567-7.
[92] Y. Xia, Y. Li, X. Wu, Q. Zhang, S. Chen, X. Ma, M. Yu, Ironing out the details: how iron orchestrates macrophage polarization, Front. Immunol. 12 (2021), 669566, https://doi.org/10.3389/fimmu.2021.669566.